On the nature of the turbulent energy dissipation energy beneath non-breaking waves

Darek J. Bogucki[1], Brian K. Haus[2], Mohammad Barzegar[1], Shao Mingming[2], Julian A. Domaradzki[3]

[1]Texas A&M University-Corpus Christi, Department of Physical and Environmental Sciences, Corpus Christi, USA
[2]University of Miami, Rosenstiel School of Marine and Atmospheric Science, Department of Ocean Sciences, USA
[3]University of Southern California, Department of Aerospace and Mechanical Engineering, USA

Key Points:

- Nonbreaking surface waves magnify background turbulent fluctuations.
- Nonbreaking wave enhanced turbulence is characterized by a relatively low Reynolds number.
- The dissipation caused by nonbreaking waves can attain values comparable to breaking surface waves.
- The dissipation caused by nonbreaking waves is proportional to the square of the mean wave flow stress tensor.

Corresponding author: Darek Bogucki, Darek.Bogucki@tamucc.edu

Abstract

Here we have determined the nature of turbulent flow associated with oceanic nonbreaking waves, which are on average much more prevalent than breaking waves in most wind conditions. We found this flow to be characterized by a low turbulence microscale Reynolds number of $30 < Re_\lambda < 100$. We observed that the turbulent kinetic energy dissipation rate associated with nonbreaking waves ϵ, ranged to $3{\cdot}10^{-4}$ W/kg for a wave amplitude 50 cm. The ϵ, under nonbreaking waves was consistent with $\epsilon = 2\nu_T \left(S_{ij}\right)^2$; S_{ij} is the large scale (energy-containing scales) wave-induced mean flow stress tensor. The turbulent Reynolds stress associated with nonbreaking waves was consistent with experimental data when parameterized by an amplitude independent constant turbulent eddy viscosity, ten times larger than the molecular value. Given that nonbreaking waves typically cover a much larger fraction of the ocean surface (90-100 percent) than breaking waves, this result shows that their contribution to wave dissipation can be significant.

Plain Language Summary

Considering that surface waves cover most of the ocean, the precise determination of the rate at which surface waves dissipate energy is necessary to properly quantify climate, weather, or ocean dynamic processes at the air-sea interface and within the upper layer of the ocean. The upper-ocean mixing intensity is often related to breaking surface waves while the turbulence generated by nonbreaking surface waves is poorly understood and thus not well represented. Our laboratory experiments used microstructure and optical measurements to observe micro velocity shears and temperature fluctuations associated with passing nonbreaking solitary surface waves. Here we report, measurements of the energy dissipation associated with these nonbreaking surface waves. We present an analytical approach to quantify the nonbreaking wave turbulence strength from large scale (energy-containing) flow measurements.

1 Introduction

In the ocean, the breaking of waves has long been thought (Terray et al., 1996; Craig & Banner, 1994) to be the dominant mechanism transferring energy from waves to the small scale turbulent flow. While the peak turbulence values observed under breaking waves are clearly much larger than in the absence of breaking, it is also the case that even in strong winds the percentage of the ocean surface covered by wave breaking is usually less than 10 percent (Anguelova & Webster, 2006). The turbulence-induced by nonbreaking surface waves (*NBSW*) was first recognized in the theoretical analysis of Phillips, (1961). He postulated that the NBSW turbulent energy dissipation level is maintained by a balance between the generation of small-scale vorticity via the large-scale vortex stretching and the losses to viscous dissipation. Ardhuin et al., (2006) derived equations for the wave energy dissipation as a result of wave-induced Stokes drift interaction with preexisting turbulence. Babanin and Haus (2009) observed NBSW turbulence in a laboratory study and found that it was intermittent, pointing to an alternative mechanism to Stokes shear. Unfortunately, it is effectively impossible to isolate NBSW turbulent dissipation in oceanic observations, where mean flows, wave breaking (Gemmrich et al., 2008), sheared wind-drift currents (Thais & Magnaudet, 1996), and buoyancy effects (Gargett et al., 1984) co-exist.

The analysis by Teixeira and Belcher (2002) demonstrated that the main mechanism responsible for NBSW turbulence is associated with Stokes drift tilting the small scale vortex structures, followed by their successive stretching. In contrast, the NBSW numerical simulations of Tsai (2015) demonstrated that the Stokes shear does not dominate the NBSW turbulence budget. The dominant energy production term was associated with the advection of turbulence by the velocity straining of waves. Recent laboratory experiments (Wang & Wijesekera, 2018) reported the observation of the NBSW

associated turbulent kinetic energy dissipations (TKED) of around 10^{-4} W/kg. Similar TKED values 20 cm below surface, were reported for plunging *breaking* waves of amplitude of 0.25 m (Wickley-Olsen et al., 2008). In this work, we have also experimentally examined the TKED associated with nonbreaking surface waves in a laboratory environment. We have demonstrated that the wave associated TKED is related to the large (energy-containing) scale wave-induced mean flow stress tensor. As a surrogate for oceanic waves, we have used a single solitary wave of varying amplitude. The soliton generation is easily controlled, and a single soliton wave enables unambiguous interpretation of measurements. Furthermore, the mechanism of the turbulence generation in an NBSW soliton via the large scale stress tensor is anticipated to be similar to one operating under oceanic NBSW.

2 Theoretical considerations

We have interpreted our results within the framework of the homogeneous and isotropic turbulent flow theory (Monin & Yaglom, 1981) because it is amenable to analytical studies while acknowledging that it is an idealized approach. The fundamental quantity in that theory is $E(k)$, the turbulent kinetic energy per unit mass. Physically, the quantity $E(k)dk$ represents contributions to the turbulent kinetic energy by the eddies, with a wavenumber k ranging between k to $k+dk$. The fluid flow total kinetic energy is then found as $u'^2 = \int_0^\infty E(k)dk$ while the amount of the viscous energy dissipation within the flow is $\epsilon = 2\nu \int_0^\infty k^2 E(k)dk$, where ν is the kinematic viscosity.

For well developed turbulent flows (characterized by a large Reynolds number) (Monin & Yaglom, 1981), the most distinctive part of the spectrum is the inertial subrange $E(k) \propto k^{-5/3}$, which in the Kolmogorov theory terminates below the Kolmogorov or dissipation wavenumber $k_k = (\epsilon/\nu^3)^{1/4} = 1/\eta$. Here the η is the Kolmogorov length scale. Experimental results (J. Domaradzki & Rogallo, 1990; J. A. Domaradzki, 1992) indicate that the inertial range terminates at wavenumbers of around $k \approx 0.1\ k_k$. Many theoretical and numerical results (J. Domaradzki & Rogallo, 1990; J. A. Domaradzki, 1992) support that beyond $k \gg 0.2k_k$, the far dissipation range, the spectrum decays rapidly as $E(k) \propto \exp(-ak/k_k)$ with $a > 0$.

2.1 Model of the NBSW generated turbulence

The total flow velocity under a soliton U_i can be partitioned as a sum of the large-scale mean u_i and a fluctuating small-scale u_i' velocity, such that the instantaneous velocity U_i is given as $U_i = u_i + u_i'$. The u_i' can be thought of as a background velocity fluctuation existing before the NBSW or soliton arrival. During the experiments, our large wave tank typically exhibited some background small-scale velocity fluctuations arising from residual mean flow motion. The situation is analogous to oceanic conditions where the upper ocean typically maintains background small-scale turbulent fluctuations arising from external forcing.

The quantity determining the production of turbulent fluctuations of $u_i'^2$, and ultimately the rates of turbulent dissipation, is the local turbulent Reynolds stress $\overline{u_i'u_j'}$ where $\overline{(\ \ )}$ denotes averaging. We can model the turbulent Reynolds stress in terms of the large-scale flow with the aid of the averaged Navier–Stokes (RANS) equations. Following the RANS $k-\epsilon$ model (Durbin, 2004), for a homogeneous and stationary turbulent flow in water, we can parameterize the local turbulent Reynolds stress $\overline{u_i'u_j'}$ by a turbulent eddy viscosity ν_T acting on the large-scale flow gradients S_{ij} as (Durbin, 2004): $-\overline{u_i'u_j'} + \frac{2}{3}\overline{u_k'u_k'}\,\delta ij \equiv 2\nu_T S_{ij}$. The mean flow strain tensor S_{ij} is given by:

$$S_{ij} \equiv \frac{1}{2}\left(\frac{\partial u_i}{\partial x_j} + \frac{\partial u_j}{\partial x_i}\right) \tag{1}$$

We further assume that in the case of NBSW generated turbulence, the local turbulent production is approximately balanced by viscous dissipation. This assertion is well supported experimentally (J. A. Domaradzki, 1992) for a wide range of turbulent flows with a low Re microscale number Re_λ. More specifically, in case of a flow with $Re_\lambda \geq 25$, it was observed that the turbulent production was mostly balanced by the viscous dissipation term. In that experiment (J. A. Domaradzki, 1992) the nonlocal energy transfer term become dominant only in the far dissipation spectral region i.e. for $k\eta > 0.2$.

With turbulent production P defined as $P \equiv -\overline{u_i' u_j'}\, S_{ij}$, then after replacing the Reynolds stress $\overline{u_i' u_j'}$ by its ν_T parametrization, we obtain a simple estimate of turbulent dissipation in terms of large-scale flow gradients as (Durbin, 2004):

$$\epsilon \approx P = 2\nu_T \left(S_{ij}\right)^2 \tag{2}$$

The relation Eq. 2 now permits us to evaluate the local TKED in terms of unknown parameter ν_T when the mean (large scale) flow associated with the wave is known.

The validity of Eq. 2, and our approach, can be verified analytically when the NBSW is traveling into the flow with no pre-existing turbulence. We expect that the analytical approach should formally converge to the expression Eq. 2 with $\nu_T = \nu$ *for any wave.*

2.2 Analytical verification of the NBSW energy dissipation model: $\epsilon \approx 2\nu_T \left(S_{ij}\right)^2$ for the laminar background flow

The lowest limit of the NBSW energy dissipation is attained when the mean flow associated with the wave is laminar and in the absence of background turbulent fluctuations. Then, we can calculate the wave dissipated energy directly from the Navier-Stokes equation *without invoking the Reynolds averaging method* used to derive Eq. 2. We then can apply a standard approach (Lamb, 1924; Landau & Lifshitz, 1959) to investigate the surface wave's decay rate for waves characterized by viscous, laminar flow, and in the absence of the surface tension. This analysis (Landau & Lifshitz, 1959) results in the *exact* expression for the energy dissipated by the wave occupying volume V. The averaged and the local dissipations $\overline{\epsilon_{irrot}}$ and ϵ_{irrot} are then respectively given as (Landau & Lifshitz, 1959):

$$\overline{\epsilon_{irrot}} \simeq \frac{\dot{E}_{\mathrm{kin}}}{M} = -\frac{2\nu}{V}\int_V \left(S_{ij}\right)^2 \mathrm{d}V \xrightarrow{V\to 0} 2\nu \left(S_{ij}\right)^2 = \epsilon_{irrot}, \tag{3}$$

where M is the wave mass. The symbol $\simeq$ reflects the fact that every surface wave is characterized by a very thin near-surface layer affected by the fluid rotation (Klettner & Eames, 2012) the presence of which, following Landau's (1959) argument, can be ignored in calculations of wave energy dissipation. The expression Eq. 2 formally converges to Eq. 3 when $\nu_T = \nu$ and it represents a lower limit of the NBSW energy dissipation when propagating over fluid with no background turbulence.

3 Experimental Method

The flow associated with any NBSW can be decomposed into three distinct layers (Klettner & Eames, 2012): a rotational boundary layer adjacent to the rigid bottom, the wave irrotational core, and the rotational layer adjacent to the free surface. The experiments of (Lin et al., 2015) demonstrated that the thickness of the bottom boundary under a passing soliton is less than 7 *cm* when scaled to our experimental conditions. Based on results from direct numerical simulations (DNS) of nonbreaking surface solitons (Klettner & Eames, 2012) we have calculated that the near-surface layer was at most a few *mm* thick in our experiments. During the soliton passage, we expect the surface boundary to be additionally weakened as the near-surface vorticity sign changes twice (Klettner & Eames, 2012). In experiments we expected the irrotational wave core to extend from 7 *cm* above the tank bottom to a few millimeters below the free surface.

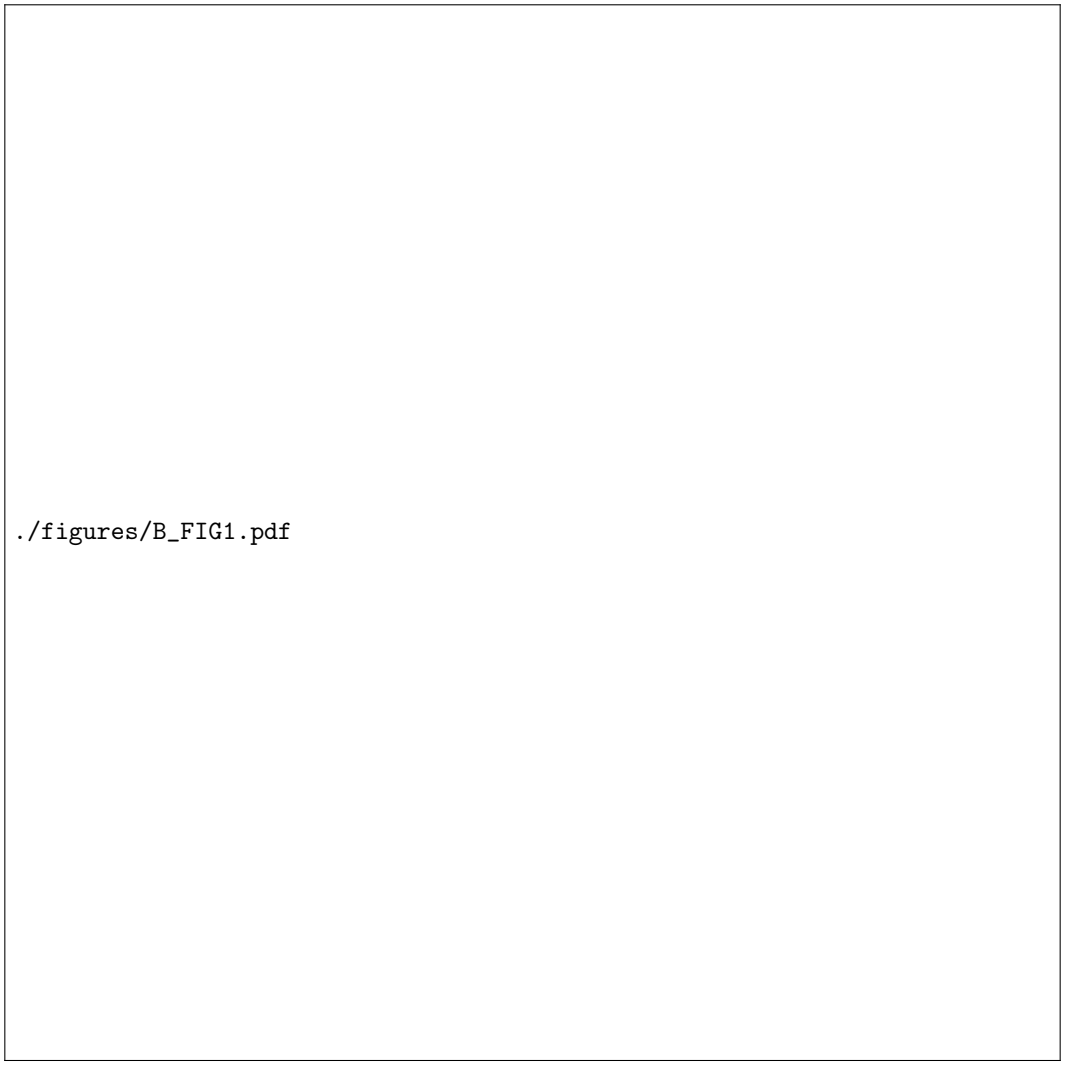

Figure 1. **A.** Schematic depiction of the experimental setup- side view. The $U_i(x, y, t)$ denotes flow components under the wave. The location of the in-water sensors and their depths in undisturbed water are shown. **B.** The VMP measured shear spectra displayed as the compensated nondimensional energy spectra $k^{5/3}E(k)$. The wavenumber k is nondimensionalized by the Kolmogorov length-scale η. The microscale Reynolds number, Re_λ, for the collected spectra was $30 < Re_\lambda < 100$. The error bar represents one standard deviation within the sample.

To examine the turbulence generated by the NBSW we have carried out a laboratory experiment with several nonbreaking single long solitary waves, Fig. 1. The experiment was carried out in the UM/RSMAS SUSTAIN facility - a wave flume of 23 m length, 6 m wide, filled to a 0.72 m depth with fresh water. The solitons were generated by a computer-controlled series of 12 piston-type hydraulic wave paddles (manufactured by HR Wallingford) located at the end of the flume. (https://sustain.rsmas.miami.edu/facility/). In each of the 40 experiments we have generated a single soliton of amplitude ranging from $a = 0.07$ to $a = 0.5$ m. Each fully formed soliton was a long surface wave with the wavelength varying between $L = 3.51$ m for the soliton of amplitude $a = 0.5$ m to $L = 9.16$ m for the smallest soliton of $a = 0.07$ m.

To avoid measurement contamination by the near-surface rotational boundary, we placed sensors at depths $0.09-0.17\ m$ below the surface, Fig. 1. The observations were carried out at $13\ m$ away from the wavemaker, a distance which permits the soliton to become fully formed (Katell & Eric, 2002). The surface elevation time series computed from pressure measurements with pressure sensors (MKS Differential Pressure Transducer model 226 A with 10 Hz acquisition speed) placed $0.13\ m$ below the undisturbed surface allowed us to calculate the soliton's properties such as amplitude a, wavelength L, and speed C, Fig. 1. The concurrent and collocated time series of the current speed was obtained with the aid of a current meter - JFE Advantech, Infinity EM AEM-USB, $10\ Hz$ acquisition speed, Fig. 1. Solitons were monitored for signs of wave breaking by analyzing the pressure and the current velocity time series from collocated sensors (Fig. 1). Comparison of depth-dependent wave-induced currents before and after the soliton passage allowed us to isolate and reject from subsequent analysis those solitons with any current asymmetries indicative of wave breaking.

Averaged measurements of the TKED under the passing solitons were carried out with a microscale shear sensor VMP200 (Macoun & Lueck, 2004). To measure the microstructure of velocity fluctuations in the cross-stream flow velocity w', we used a shear probe (R. G. Lueck et al., 2002) VMP200 (Rockland Inc.). The instrument processing electronics ($512\ Hz$ sampling frequency) generate a signal proportional to $\partial w'/\partial x$ converted to $\Psi(k)$, the velocity shear spectrum (Macoun & Lueck, 2004) when the flow velocity is known and constant. The VMP200 was mounted horizontally and pointing in the x-direction, Fig. 1. The VMP200 was equipped with two independent shear probes - separated vertically by $8\ cm$ in our experiments. The shear probe closest to the surface was located at $9\ cm$ from the undisturbed water level, Fig. 1. $\Psi(k)$ can then be related to the spatial spectrum of the turbulent kinetic energy as $E(k) = \frac{15}{4}\Psi(k)/k^2$ (R. Lueck, 2014).

In each run, the turbulent kinetic energy dissipation ϵ, was found following (R. Lueck, 2014). The $\epsilon = (C_k\, k^{5/3} E(k))^{3/2}$ was directly plotted with the Kolmogorov constant $C_k = 1.5$ for the range of wavenumbers. In the analysis of the VMP200 data, for each soliton, we used a dataset of $0.2\ sec$ duration, coinciding with the soliton peak. At the peak, the wave-induced current attained its maximum speed and exhibited minimal velocity variability. The $0.2\ sec$ long time series of $E(k)$ were then used in subsequent analysis.

An Optical Turbulence Sensor (D. J. Bogucki & Domaradzki, 2015) (OTS), Fig. 1 was also used to observe TKED over scales short enough to resolve phase-dependent fluctuations. As configured for this experiment the OTS acquired 10000 temperature gradient spectra per second. The spectra averaged over $0.01\ sec$, following (D. Bogucki et al., 1997), were then used to obtain the TKED. The OTS (D. J. Bogucki et al., 2007; D. J. Bogucki & Domaradzki, 2015) enabled phase-resolved TKED measurements associated with the soliton. The OTS is also suitable for low Re_λ flow measurements as it relies on information about turbulence temperature spectra from around the temperature dissipation peak and the far dissipation spectral region (D. J. Bogucki & Domaradzki, 2015).

The OTS measured temperature gradient spectra (D. J. Bogucki et al., 2007) and the light intensity. The OTS (D. J. Bogucki et al., 2007; D. J. Bogucki & Domaradzki, 2015) generated a light sheet parallel to NBSW wave crests. The light sheet, after propagating through the analyzed portion of the flow and over $0.5\ m$ pathlength was imaged by the OTS line-scan camera (Piranha 2, DALSA, size 8192 pixels each $7\ \mu m$, (total length of $6\ cm$) with an acquisition speed of $10,000\ lines/second$. As the water passed by the OTS, its line scan camera recorded the light intensity reported here, Fig. 2, as a 2D distribution of light intensity with the horizontal axis corresponding to the acquisition time, and the vertical axis is the position along to the OTS light sheet. That created image of light intensity, Fig. 2, similar to a shadowgraph technique (Barnes & Bellinger, 1945)

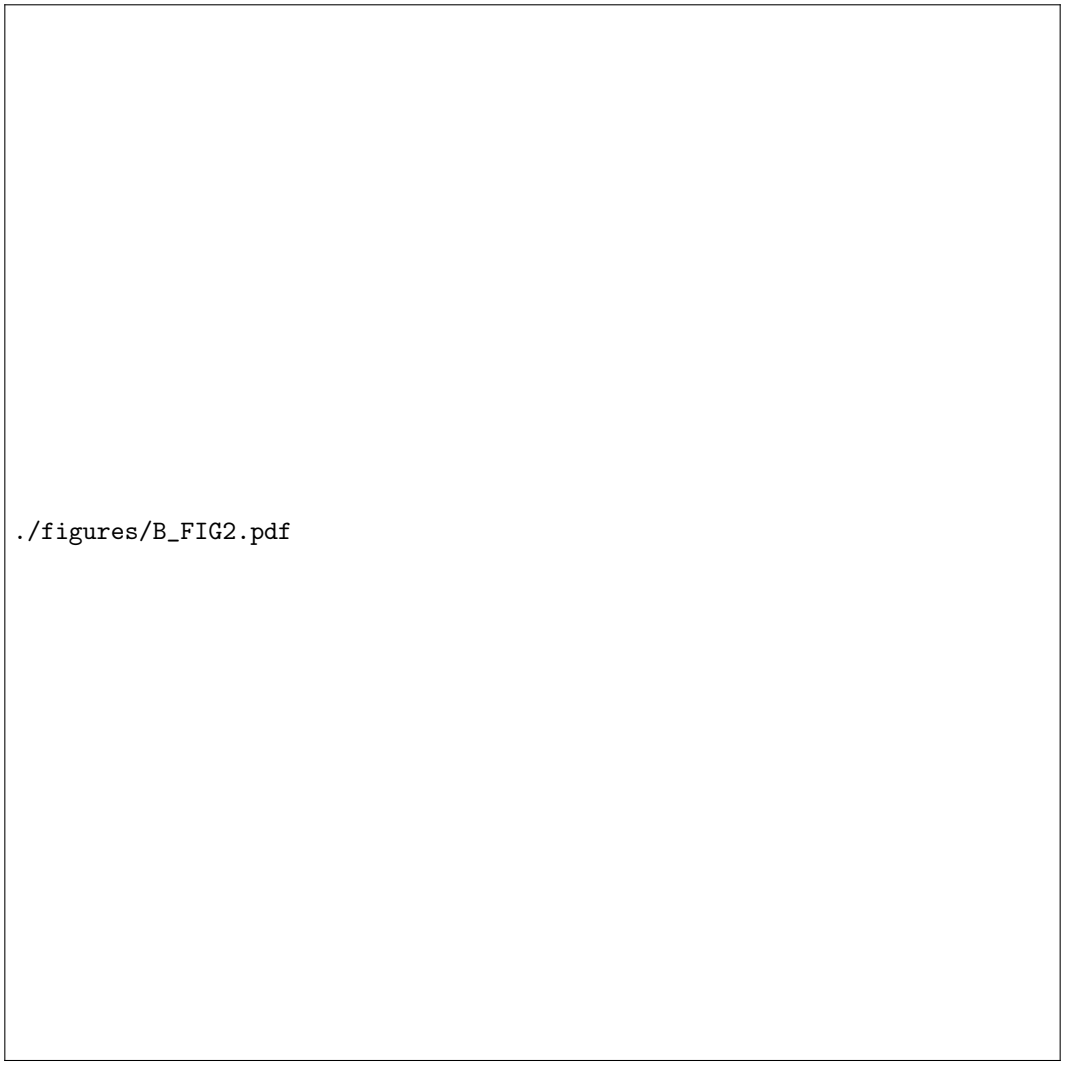

Figure 2. The shadowgraph image of the evolution of a layer. The horizontal axis is time in pixels related to flow speed passing the stationary line camera; the vertical axis is the distance in pixels.

used to reveal non-uniformities in transparent media, allowed us to visualize the small scale refractive index structures. The time-stamped OTS data, collocated with current meter and pressure sensors, were then used in ensuing analysis.

In our experiments, the water refractive index was a function of the water temperature. Consequently, the OTS observed light intensity variability was associated with the distribution of the temperature turbulent structures and the underlying strength of the refractive index gradient. An example shadowgraph image shown during the passage of a soliton reveals the structure of the local temperature gradients (Figure 2). The sequence of events is as follows: 0.2 *sec* before the wave peak of S_{ij}^2 attains a maximum. 0.2 *sec* prior to the peak the layer starts increasing with the increase of local temperature gradients. At around 0.1 *sec* past, the peak the layer thickness and local temperature gradients are the largest, and soon after the layer disappears. The 0.2 *sec* past the wave peak S_{ij}^2 attains second maximum - likely contributing to the layer demise.

4 Results

4.1 Evidence of Turbulence Generated by Nonbreaking Surface Waves

The shear sensor derived $E(k)$ data, for all runs, are presented in the form of a dimensionless compensated energy spectrum $k^{5/3}E(k)$, Fig. 1. The energy spectrum $E(k)$ generated by passing NBSW, Fig. 1, exhibited a short inertial spectral range where $E(k) \propto k^{-5/3}$ for $k\eta < 0.1$, followed by a tail of rapidly decaying kinetic energy $E(k)$. The measured $E(k)$ spectra can be compared to equivalent ones (J. A. Domaradzki, 1992) obtained in DNS of turbulent flows when characterized by a similar value of their microscale Reynolds number Re_λ.

The Re_λ physically represents a ratio of local small-scale turbulent stress to the mean flow viscous stress (Tennekes et al., 1972), and its larger value indicates a longer extent of the inertial range. For each soliton, the $Re_\lambda = u'\lambda/\nu$ was calculated from a time series of velocity fluctuation u' over 0.2 seconds interval around the soliton peak. The Taylor microscale lengthscale (Tennekes et al., 1972) can be found as: $\lambda = u'\sqrt{15\nu/\epsilon}$. We estimated that the microscale Reynolds number covered the range $30 < Re_\lambda < 100$ around the soliton peak and for the range of the measured soliton amplitudes. The estimated low Re_λ associated with the NBSW is consistent with observed $E(k)$ spectra, Fig. 1. and with the numerical simulations for a variety of turbulent flows (J. Domaradzki & Rogallo, 1990; J. A. Domaradzki, 1992). The DNS experiment (D. Bogucki et al., 1997) with $Re_\lambda = 77$ demonstrated that the $E(k)$ inertial range was restricted to wavenumbers $0.025 < k\eta < 0.1$ in line with our observation, Fig. 1. The low Reynolds number turbulent flow generated by NBSW was observed in numerical experiments of Tsai (2015).

The existence of low Re number turbulent flow generated by an NBSW with a short inertial range has a far-reaching consequence as the typical oceanic turbulence (Jiménez, 1998) is typically characterized by a large microscale Reynolds number of a $Re_\lambda \simeq 1000$. It is not very clear that large Reynolds number turbulence models currently incorporated in a host of near-surface oceanic models can be easily adaptable to the NBSW flows with a low Reynolds number. For example, recent (Zhuang et al., 2020) attempts to incorporate NBSW generated turbulence was based on large Reynolds turbulence models and such efforts may not accurately reflect the underlying physical processes such as NBSW mixing, vertical momentum, and scalar transfer or the wave energy dissipation.

4.2 Mechanism of nonbreaking wave turbulence generation

In line with the arguments of (Teixeira & Belcher, 2002; Tsai et al., 2015), and based on our observations presented here, *we posit that the turbulent flow associated with the passing NBSW, was a result of the amplification of background turbulent velocity fluctuations existing before wave arrival.* That intensification is accomplished by the action of large-scale laminar flow velocity gradients on pre-existing small scale turbulent fluctuations as observed in simulations (Tsai et al., 2015). We can elucidate some details of this preexisting turbulence amplification mechanism with the aid of the OTS (Fig. 2) observations as follows:

During the soliton passage, at the wave peak, the wave-induced mean flow was directed away from the wavemaker with a mean flow speed approaching 0.7 m/s for a wave of amplitude $a = 0.5$ m, Fig. 4. Fig. 2 displays the light intensity time series along a 4 cm long line segment, over a 0.6 sec time interval centered at the soliton peak, for a soliton of amplitude $a = 0.5$ m. In the image, Fig. 2, before the soliton peak, we noticed the appearance of a thin layer-like structure, characterized by a time-varying thickness. That layer was denoted in Fig. 2 by its thickness at a peak of 2.1 mm. Before the soliton peak arrival, the layer commenced as a very thin $\ll 1$ mm thick structure, becoming 2.1 mm thick at a wave peak and disappearing $\simeq 0.1$ sec later. Concurrently,

with the change of the layer thickness, and before the soliton peak (Fig. 2), we noted the increase of light gradient intensity related to an increase of the refractive index, which in turn was proportional to the increase of the local temperature gradient (Barnes & Bellinger, 1945).

The structure evolution is thus characterized by changes in its size and associated temperature gradient. It started as a thin layer with a relatively weak temperature gradient, but past the wave peak, the layer attained its maximum thickness and the largest temperature gradients, then the layer rapidly disappeared. We attribute the sudden layer disappearance to the viscous dissipation acting on very strong local density gradients. We posit that the small-scale velocity gradients likely follow a similar path with the small-scale vortex, stretching and driving the turbulent energy cascade (Davidson et al., 2008). The observed NBSW turbulence generation is consistent with that of the wave mean flow magnifying local preexisting turbulent flow.

5 Estimation of turbulent viscosity ν_T, associated with turbulent flow generated by long surface solitary waves.

To estimate the value of the ν_T associated with the NBSW solitons we compared the prediction of Eq. 2 against measured values of ϵ. In principle, we could experimentally measure all components of S_{ij}, see Eq. 1, but such an approach was highly impractical. Instead, we used a modeled large-scale mean flow generated by the NBSW wave to deduce the S_{ij} components. The experiment runs were executed in constant intervals. The residual tank flow was thus assumed to be similar for every run. We then, for simplicity, assume that the background velocity fluctuations in each run were the same.

To calculate the mean flow strain tensor S_{ij} from Eq. 1, we need an analytical expression for the soliton horizontal and vertical current components u and v respectively, along with estimates of wave speed C and its length L. We have chosen the analytical soliton representation of Wiegel (2013), which is accurate to the 3-rd order in the non-dimensional wave amplitude a/d. That approach agrees the most favorably with a number of laboratory measurements of several soliton characteristics (Wiegel, 2013). In the case of wave speed, it agrees with experiments up to wave amplitudes $a/d < 0.72$, which was larger than our largest analyzed soliton of $a/d = 0.69$. Third-order accurate expressions for the surface soliton elevation $y_s(x, t = 0)$ and the speed are (Wiegel, 2013), $\frac{C}{\sqrt{gd}} = 1 + \frac{1}{2}\frac{a}{d} - \frac{3}{20}\left(\frac{a}{d}\right)^2 + ...$, and with $A_\omega \equiv \frac{1}{d}\sqrt{(\frac{3a}{4d})}[1 - \frac{5a}{8d}]$ at $t = 0$ we have (Wiegel, 2013): $y_s = d + a\,\mathrm{sech}^2(A_\omega x) - \frac{3}{4}a\left(\frac{a}{d}\right)\mathrm{sech}^2(A_\omega x)[1 - \mathrm{sech}^2(A_\omega x)]$. The horizontal and vertical mean current components generated by a passing wave evaluated at the (x, y) location are respectively given (Wiegel, 2013):

$$\frac{u}{\sqrt{gd}} = \frac{a}{d}\left[1 + \frac{1}{4}\frac{a}{d} - \frac{3}{2}\frac{a}{d}\frac{y^2}{d^2}\right]\mathrm{sech}^2(A_\omega x) + \left(\frac{a}{d}\right)^2\left[-1 + \frac{9}{4}\frac{y^2}{d^2}\right]\mathrm{sech}^4(A_\omega x), \tag{4}$$

and for the vertical velocity:

$$\begin{aligned}\frac{v}{\sqrt{gd}} =& \sqrt{3}\left(\frac{a}{d}\right)^{3/2}\left(\frac{y}{d}\right)\mathrm{sech}^2(A_\omega x)\tanh(A_\omega x) \\ &\cdot\left[1 - \frac{3}{8}\frac{a}{d} - \frac{1}{2}\frac{a}{d}\frac{y^2}{d^2} + \frac{a}{d}\left(-2 + \frac{3}{2}\frac{y^2}{d^2}\right)\mathrm{sech}^2(A_\omega x)\right]^s\end{aligned} \tag{5}$$

From the pressure sensor data for each soliton, we measured the wave amplitude a, then with the aid of Eqs. (1, 4, 5) we calculated S_{ij} as a function of the soliton amplitude a. We then found ν_T by the fitting the VMP200 measured TKED to the ϵ estimate given by Eq. 2 for each measured soliton. Fig. 3 displays the shear sensor measured TKED and the turbulent dissipation modeled by Eq. 2. By fitting Eq. 2 to our data, we found that $\nu_T = 10\nu$ is the best approximation. The modeled and measured

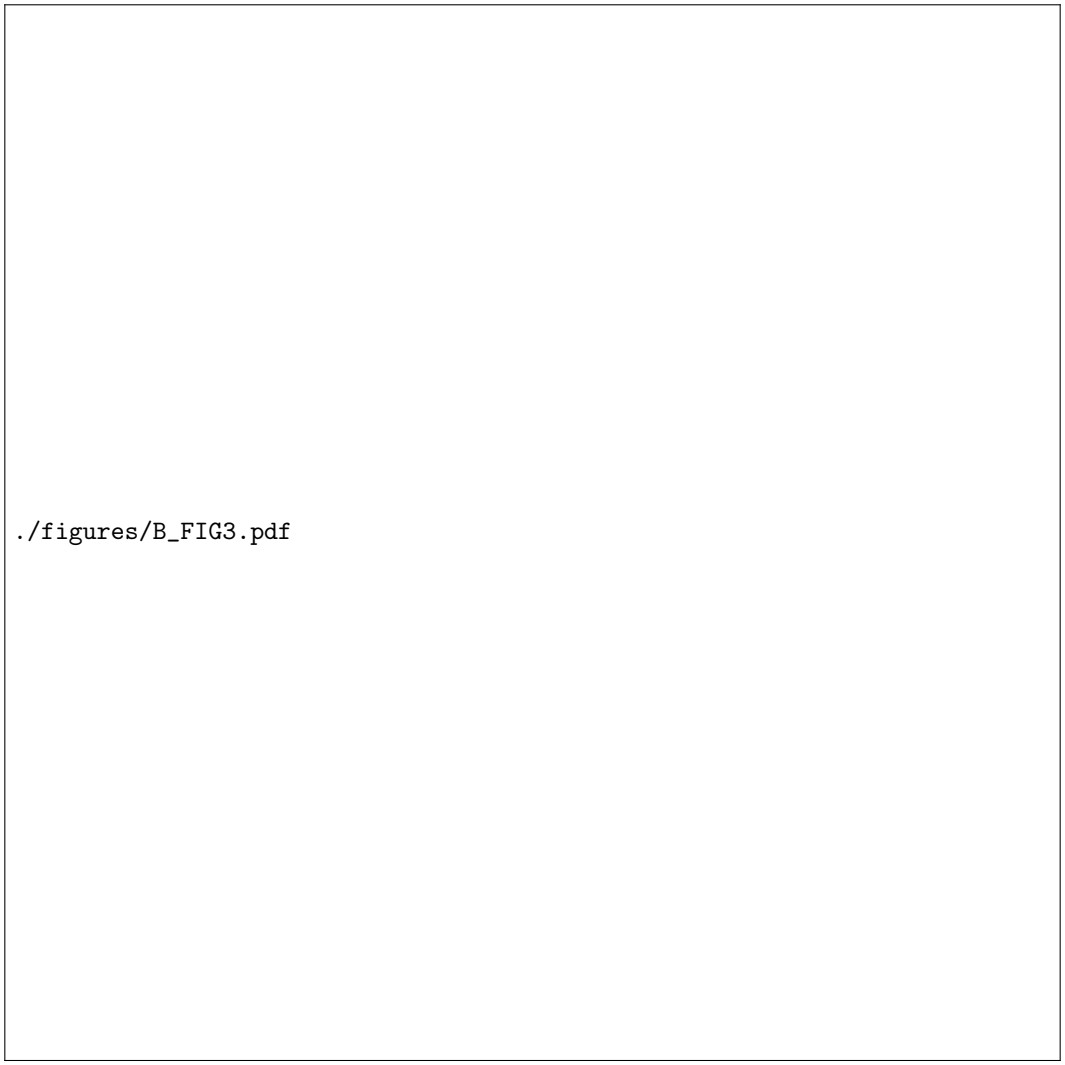

Figure 3. The TKED measured by the VMP200 and averaged over 0.2 *sec* around the soliton peak. The red/black dots correspond to shear probe located at ($y = 0.55$ / $y = 0.63$) m respectively above bottom. The thin blue and thick black lines correspond to theoretical dissipation estimates based on the strength of the wave mean flow stress tensor S_{ij}^2, Eq. 2 and Eq. 4. The error bar represents 1 standard deviation within the sample.

dissipations are displayed as a function of wave amplitude, Fig. 3. Most of our measured TKED values were consistent with the constant and wave amplitude independent eddy viscosity $\nu_T = 10\nu$. We attributed large scatter of measured ϵ to be a likely variability of the background velocity fluctuation u'.

The observed TKED increase with wave amplitude shown in Fig. 3 was in line with the numerical experiments of Tsai (2015). We include in Fig. 3, the lowest TKED set by $\nu_T = \nu$, and associated with NBSW propagating into flow with no background velocity fluctuations Eq. 3. Information about the variability of the NBSW generated TKED can be gathered by comparing the data from two shear probes mounted on the VMP200 and separated by an 8 *cm* depth, Fig. 1. Within the range of measured wave amplitudes, the near-surface shear sensor consistently exhibited larger TKED values, Fig. 3 when compared with the deeper mounted shear sensor. That was consistent with the dissipa-

tion obtained from Eq. 2 and it reflects the fact that the mean flow stress tensor, Eq. 1 increases as we approach the surface.

To observe how the predicted TKED (Eq. 2) varied with depth, we have mapped the TKED as a function of time and depth-for a soliton of amplitude $a = 0.5\ m$. Under the wave peak, the modeled TKED (Fig. 4) intensifies as we approach the surface, with the TKED distributed symmetrically around the wave peak. Interestingly, the near-surface TKED values reveal a local TKED minimum right under the wave peak.

6 Phase dependence of the soliton generated energy dissipation.

The shear sensor could not be used for the wave phase-resolved TKED measurements due to its sensitivity to changes in the mean flow direction exhibited by a passing wave. For that task, we have used the OTS (D. J. Bogucki & Domaradzki, 2015) to elucidate the wave phase TKED dependence.

For the soliton phase-resolved TKED measurements, we have chosen a soliton with an amplitude of $a = 0.5\ m$ (case LL). Its large generated dissipation allowed for concurrent and accurate TKED measurements by both the OTS and shear sensor. The results were presented in Fig. 4, where we presented the OTS derived TKED overlaid with measured current speed. The measured TKED displays a pronounced TKED double maximum, which we have noted in several OTS soliton observations for a range of wave amplitudes.

The OTS measured TKED was within the range of shear sensor values and was consistent with the model estimate Eq. 2 with $\nu_T = 10\nu$, (Fig. 4). The double peak in ϵ is a result of the strain rate of S_{ij}^2, attaining maximum symmetrically around the wave peak. That timing was consistent with the mechanism of the large-scale strain amplifying local small-scale features.

7 Conclusions

Ocean surface waves are the most ubiquitous feature of the marine landscape. However, very little is known about how they dissipate their energy, although it has largely been attributed to the intermittent occurrence of wave breaking. Until recently, the existence of non-breaking wave-induced turbulence had been given little attention, although its presence has been suggested by the observations. However, parameterizations of wave-induced mixing in models remains a challenge. The presence of NBSW turbulence, previously not accounted for, can affect the rate of wave energy dissipation, properties of the surface boundary layer as shown by theoretical (Ardhuin & Jenkins, 2006) and numerical studies (Qiao et al., 2004; Fan & Griffies, 2014).

Our work presented here is an attempt to shed light on the details of the NBSW turbulence, thereby enabling the incorporation of the observed low Re number turbulence physics into more realistic global oceanic models. This is particularly important because the nearly ubiquitous presence of NBSW is likely responsible for a significant portion of the upper ocean vertical transport processes (Bao et al., 2020). Our observations demonstrated that the turbulent dissipation under nonbreaking waves varied with wave phase and distance from the free surface, and that it was consistent with $\epsilon = 2\nu_T \left(S_{ij}\right)^2$; where S_{ij} is the large (energy-containing) scale wave-induced mean flow stress tensor. The analytical argument resulting in equations Eq. 2, Eq. 3 suggest that our result is valid for any surface wave.

Based on our observations we posit that the turbulent flow associated with passing NBSW was a result of the amplification of the background turbulent velocity fluctuations and consistent with (Teixeira & Belcher, 2002; Tsai et al., 2015) results. Future work will focus on exploring the background turbulence strength relationship with

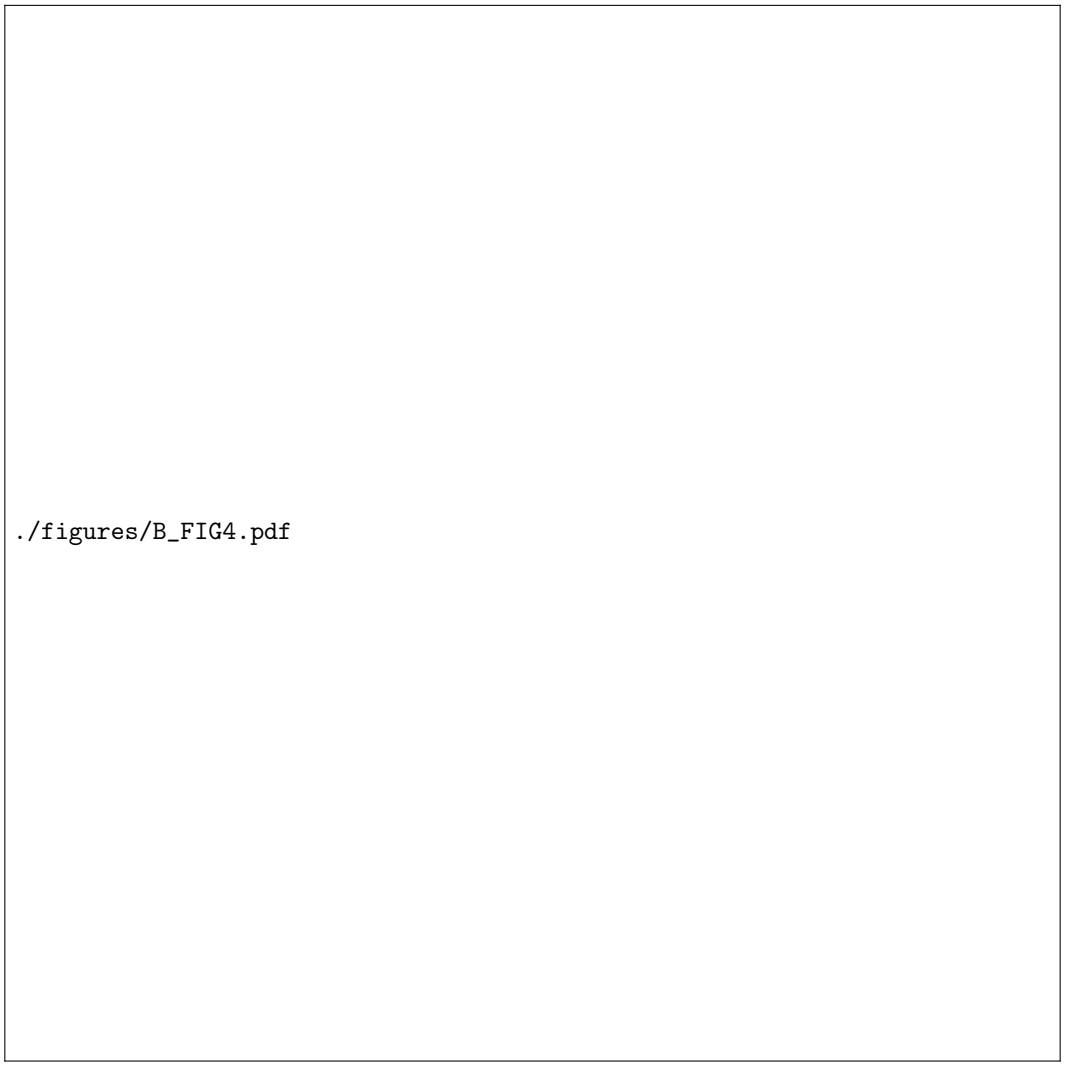

Figure 4. **A.** TKED calculated from the Eq. 3 with $\nu_T = 10\nu$, for a soliton with $a = 0.5$ m. Note that the maximum dissipation and the S_{ij}^2 is $\approx$ 0.2 second before and after soliton peak - consistent with shadowgraph observation in the Fig. 2. **B.** Measured vs. predicted at 0.55 m above the bottom: the OTS measured TKED (black) dissipation as a function of time with superimposed current speed (red) -solid lines. Dashed black line: calculated TKED dissipation from the Eq. 3 with $\nu_T = 10\nu$, for a soliton with $a = 0.5$ m. Dashed red line: measured current speed. The OTS measured maximum dissipation is attained at ≈ 0.6 *sec* before and after the soliton peak. Note fluctuations of the background dissipation before the soliton arrival.

the NBSW effective eddy viscosity and effects of stratification on the NBSW vertical mixing.

Acknowledgments

This research was made possible in part by a grant from The Gulf of Mexico Research Initiative and in part by and the National Science Foundation grant 1434670. Thanks are given to all those who worked on the tank experiment, in particular Mike Rebozo and Neil Williams.

Data are publicly available through the Gulf of Mexico Research Initiative Information and Data Cooperative (GRIIDC) at: https://data.gulfresearchinitiative.org/data/R6.x806.000:0029 (DOI:10.7266/ATC4NDEF) or https://data.gulfresearchinitiative.org and search term: R6.x806.000:0029.

References

Anguelova, M. D., & Webster, F. (2006). Whitecap coverage from satellite measurements: A first step toward modeling the variability of oceanic whitecaps. *Journal of Geophysical Research: Oceans*, *111*(C3).

Ardhuin, F., & Jenkins, A. D. (2006). On the interaction of surface waves and upper ocean turbulence. *Journal of physical oceanography*, *36*(3), 551–557.

Babanin, A. V., & Haus, B. K. (2009). On the existence of water turbulence induced by nonbreaking surface waves. *Journal of Physical Oceanography*, *39*(10), 2675–2679.

Bao, Y., Song, Z., & Qiao, F. (2020). Fio-esm version 2.0: Model description and evaluation. *Journal of Geophysical Research: Oceans*, *125*(6), e2019JC016036.

Barnes, N. F., & Bellinger, S. L. (1945). Schlieren and shadowgraph equipment for air flow analysis. *JOSA*, *35*(8), 497–509.

Bogucki, D., Domaradzki, A., & Yeung, P. K. (1997). Direct numerical simulations of passive scalars with Pr> 1 advected by turbulent flow. *J. Fluid Mech.*, *343*, 111–130.

Bogucki, D. J., & Domaradzki, J. A. (2015). Temperature gradient spectra and temperature dissipation rate in a turbulent convective flow. *Journal of Turbulence*, *16*(12), 1179–1198.

Bogucki, D. J., Domaradzki, J. A., Anderson, C., Wijesekera, H., Zaneveld, R., & Moore, C. (2007). Optical measurement of rates of dissipation of temperature variance due to oceanic turbulence. *Optics Express*, *15*(12), 7224–7230.

Craig, P. D., & Banner, M. L. (1994). Modeling wave-enhanced turbulence in the ocean surface layer. *Journal of Physical Oceanography*, *24*(12), 2546–2559.

Davidson, P., Morishita, K., & Kaneda, Y. (2008). On the generation and flux of enstrophy in isotropic turbulence. *Journal of Turbulence*(9), N42.

Domaradzki, J., & Rogallo, R. (1990). Local energy transfer and nonlocal interactions in homogeneous, isotropic turbulence. *Phys. Fluids A*, **2**, 413.

Domaradzki, J. A. (1992). Nonlocal triad interactions and the dissipation range of isotropic turbulence. *Phys. Fluids A*, *4*, 2037–2045.

Durbin, P. A. (2004). Turbulence closure models for computational fluid dynamics. *Encyclopedia of Computational Mechanics*.

Fan, Y., & Griffies, S. M. (2014). Impacts of parameterized langmuir turbulence and nonbreaking wave mixing in global climate simulations. *Journal of Climate*, *27*(12), 4752–4775.

Gargett, A., Osborn, T., & Nasmyth, P. (1984). Local isotropy and the decay of turbulence in a stratified fluid. *J. Fluid Mech.*, *144*, 231–280.

Gemmrich, J. R., Banner, M. L., & Garrett, C. (2008). Spectrally resolved energy dissipation rate and momentum flux of breaking waves. *J. Phys. Oceanogr.*, *38*(6), 1296–1312.

Jiménez, J. (1998). Oceanic turbulence at millimeter scales. *Oceanographic Literature Review*, *3*(45), 598.

Katell, G., & Eric, B. (2002). Accuracy of solitary wave generation by a piston wave maker. *Journal of Hydraulic Research*, *40*(3), 321–331.

Klettner, C. A., & Eames, I. (2012). The laminar free surface boundary layer of a solitary wave. *Journal of Fluid Mechanics*, *696*, 423–433.

Lamb, H. (1924). *Hydrodynamics*. University Press.

Landau, L., & Lifshitz, E. (1959). *Vol 6: Fluid mechanics*. Addison-Wesley Mass.

Lin, C., Yu, S.-M., Yeh, P.-H., Yu, M.-H., Tsai, C.-P., Hsieh, S.-C., ... Raikar, R. (2015). Characteristics of boundary layer flow induced by solitary wave propagating over horizontal bottom. *Journal of Marine Science and Technology*, *23*(6), 909–922.

Lueck, R. (2014). Rsi technical note 030: On the forms of the velocity, shear, and rate-of-strain spectra. *Victoria, BC, Canada: Rockland Scientific Inter-*

national. Retrieved from http://rocklandscientific. com/support/knowledge-base/technical-notes.

Lueck, R. G., Wolk, F., & Yamazaki, H. (2002). Oceanic velocity microstructure measurements in the 20th century. *Journal of Oceanography*, *58*(1), 153–174.

Macoun, P., & Lueck, R. (2004). Modeling the spatial response of the airfoil shear probe using different sized probes. *Journal of Atmospheric and Oceanic Technology*, *21*(2), 284–297.

Monin, A. S., & Yaglom, A. M. (1981). *Statistical Fluid Mechanics: Mechanics of Turbulence*. The MIT press.

Phillips, O. (1961). On the dynamics of unsteady gravity waves of finite amplitude part 2. local properties of a random wave field. *J. Fluid Mech.*, *11*(1), 143–155.

Qiao, F., Yuan, Y., Yang, Y., Zheng, Q., Xia, C., & Ma, J. (2004). Wave-induced mixing in the upper ocean: Distribution and application to a global ocean circulation model. *Geophysical Research Letters*, *31*(11).

Teixeira, M., & Belcher, S. (2002). On the distortion of turbulence by a progressive surface wave. *Journal of Fluid Mechanics*, *458*, 229–267.

Tennekes, H., Lumley, J. L., Lumley, J. L., et al. (1972). *A first course in turbulence*. MIT press.

Terray, E. A., Donelan, M., Agrawal, Y., Drennan, W. M., Kahma, K., Williams, A. J., ... Kitaigorodskii, S. (1996). Estimates of kinetic energy dissipation under breaking waves. *Journal of Physical Oceanography*, *26*(5), 792–807.

Thais, L., & Magnaudet, J. (1996). Turbulent structure beneath surface gravity waves sheared by the wind. *J. Fluid Mech.*, *328*, 313–344.

Tsai, W.-t., Chen, S.-m., & Lu, G.-h. (2015). Numerical evidence of turbulence generated by nonbreaking surface waves. *Journal of Physical Oceanography*, *45*(1), 174–180.

Wang, D. W., & Wijesekera, H. W. (2018). Observations of breaking waves and energy dissipation in modulated wave groups. *Journal of Physical Oceanography*, *48*(12), 2937–2948.

Wickley-Olsen, E., Boufadel, M. C., King, T., Li, Z., Lee, K., & Venosa, A. D. (2008). Regular and breaking waves in wave tank for dispersion effectiveness testing. In *International oil spill conference* (Vol. 2008, pp. 499–508).

Wiegel, R. L. (2013). *Oceanographical engineering*. Courier Corporation.

Zhuang, Z., Zheng, Q., Yuan, Y., Yang, G., & Zhao, X. (2020). A non-breaking-wave-generated turbulence mixing scheme for a global ocean general circulation model. *Ocean Dynamics*, *70*(3), 293–305.

Figure 1.

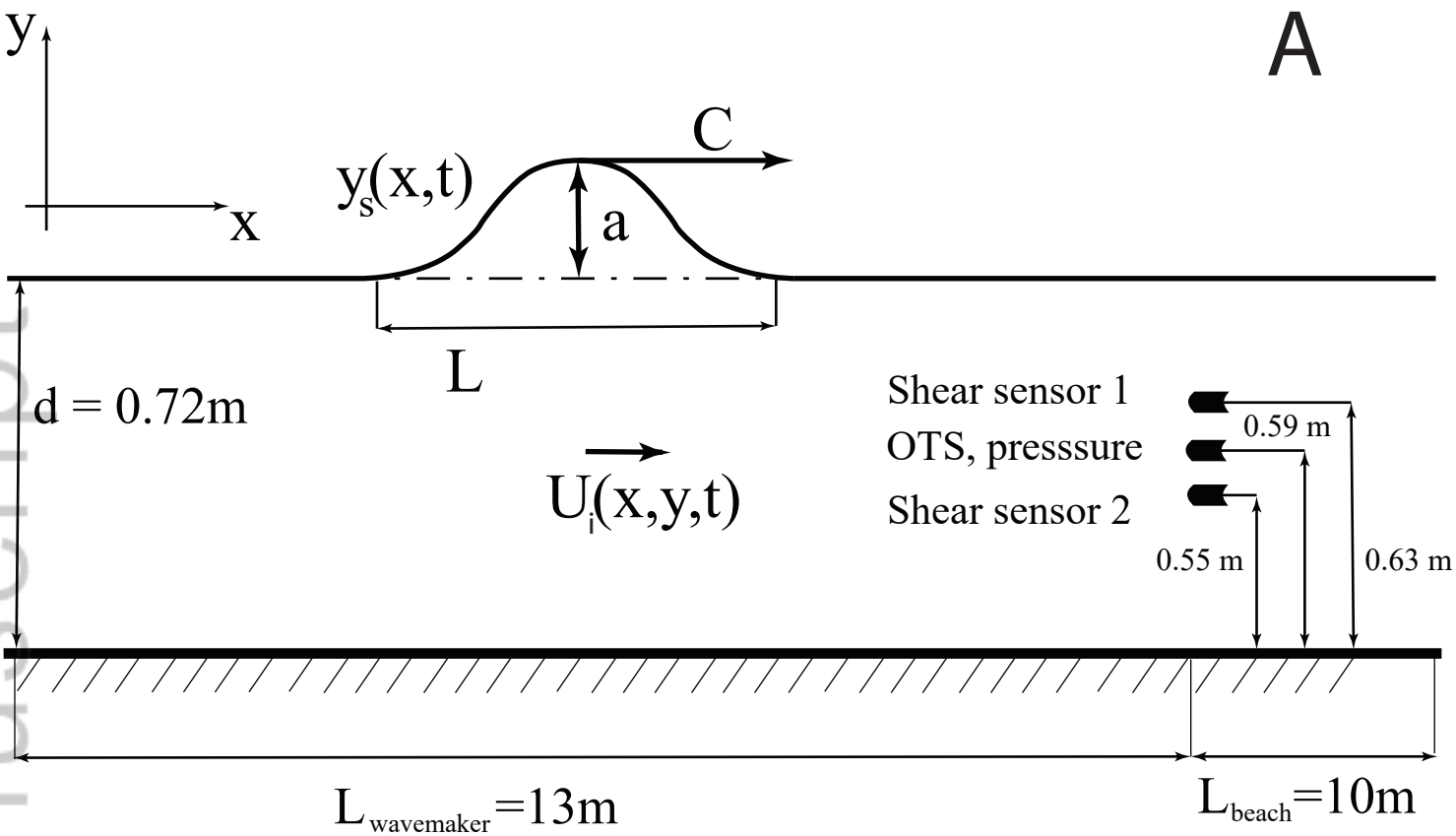

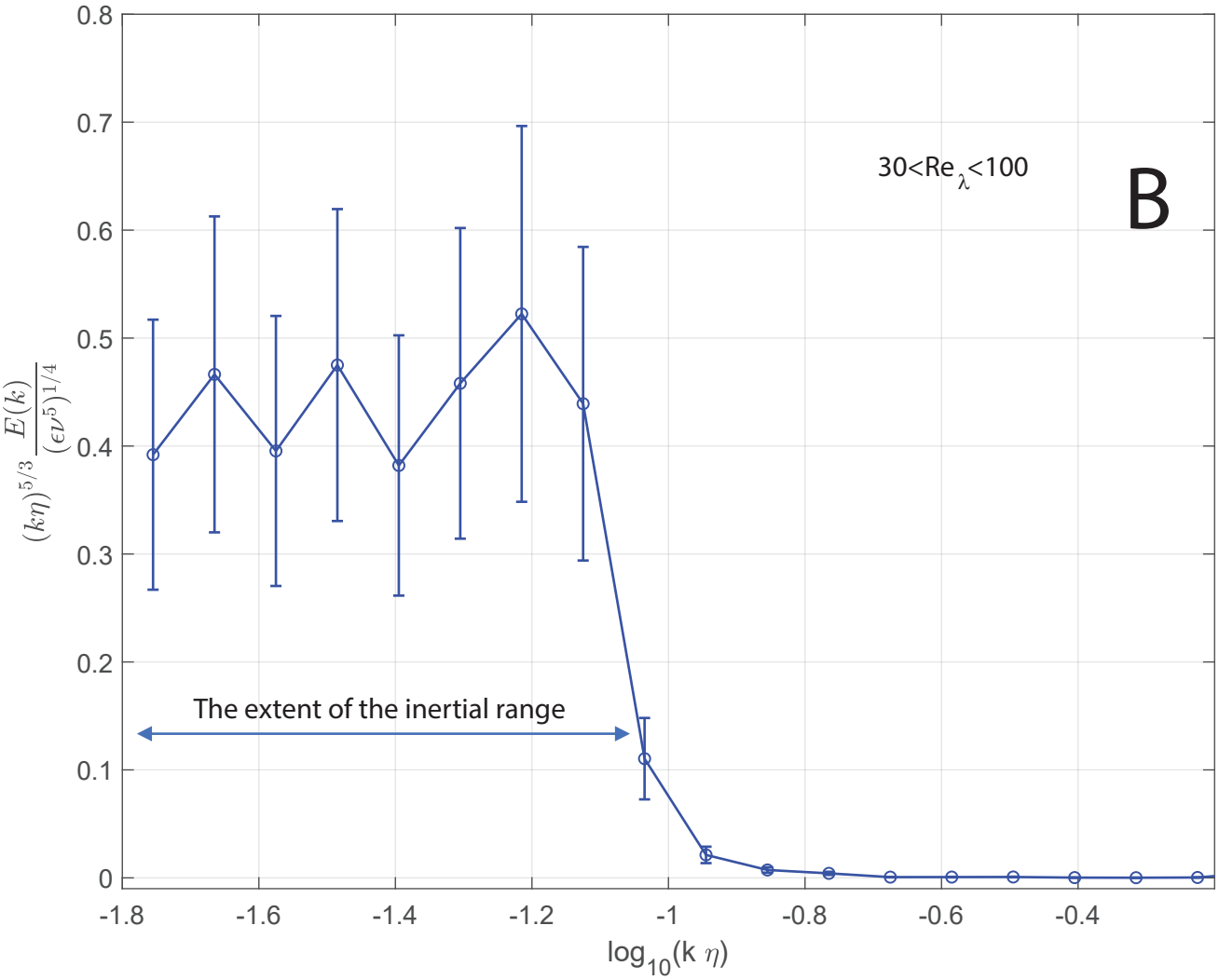

Figure 2.

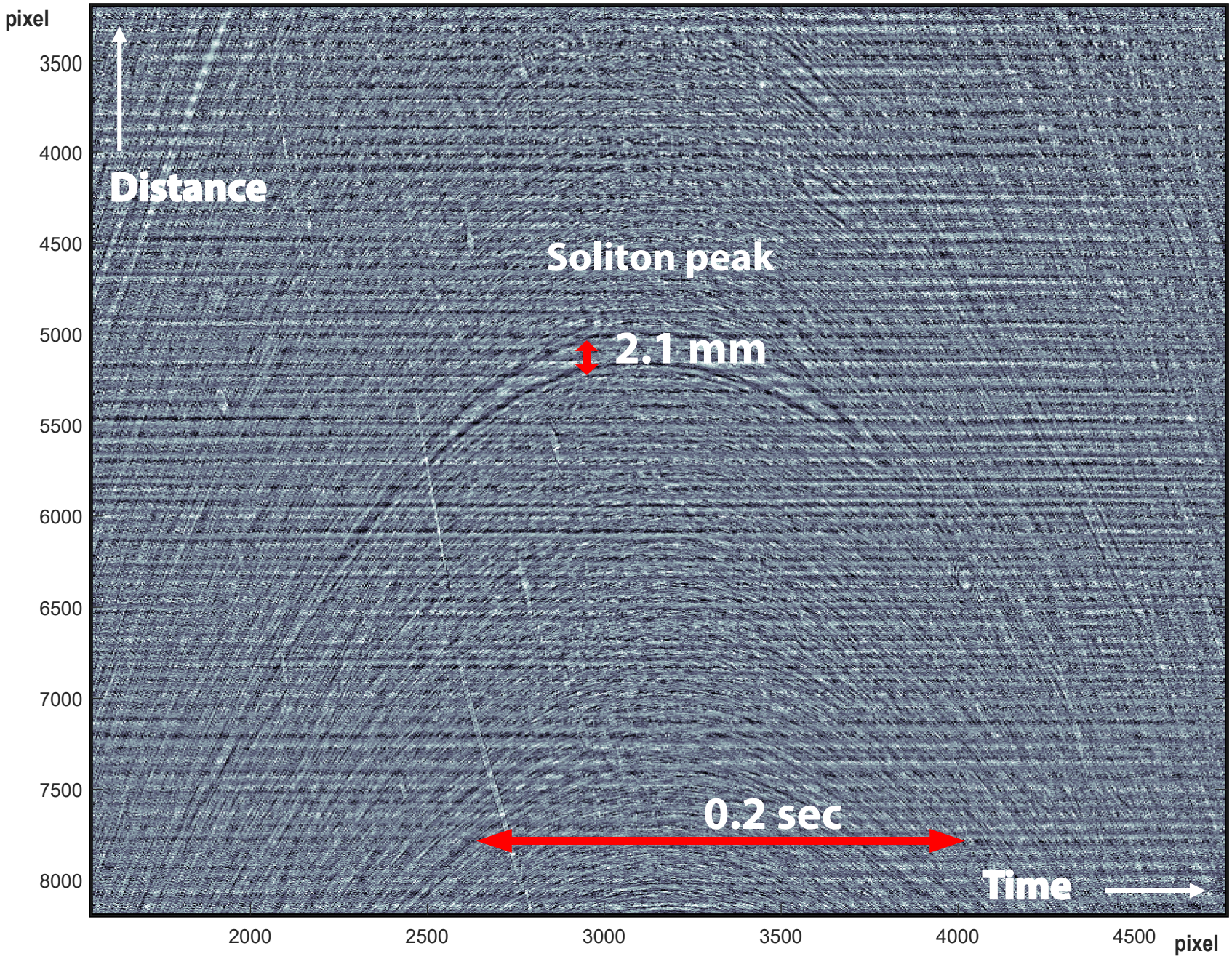

Figure 3.

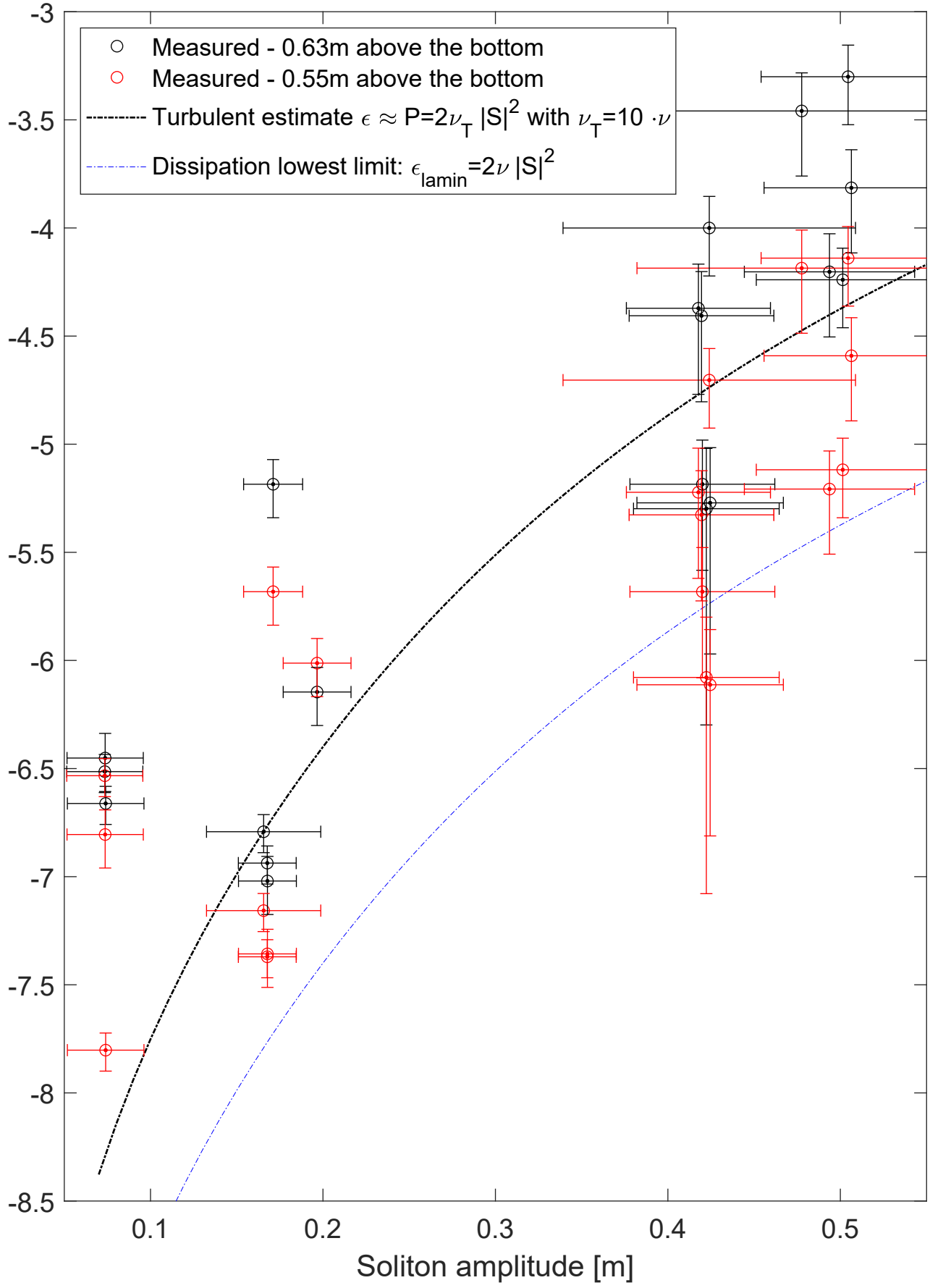

Figure 4.